Sputtered nickel oxide on vertically-aligned multiwall carbon nanotube arrays for lithium-ion batteries

Rahmat Agung Susantyoko[a,b], Xinghui Wang[b], Qizhen Xiao[b], Eugene Fitzgerald[a,c] and Qing Zhang[1a,b]

[a] Advanced Materials for Micro- and Nano- Systems, Singapore-MIT Alliance, Singapore 637460, Singapore.

[b] School of Electrical and Electronic Engineering, Nanyang Technological University, Singapore 639798, Singapore.

[c] Department of Materials Science and Engineering, Massachusetts Institute of Technology, Cambridge, Massachusetts 02139, USA.

[1] Corresponding author. Tel.: +65 6790 5061. Fax: +65 6793 3318. E-mail address: eqzhang@ntu.edu.sg (Q. Zhang).

Abstract:

We fabricated nickel oxide (NiO) on vertically-aligned multiwall carbon nanotube (MWCNT) arrays (MWCNT/NiO) as an electrode for lithium-ion batteries. The specific capacity of 864.8 mA h g^{-1} at the rate of 143.6 mA g^{-1} for up to 50 cycles was achieved. Compared to the electrode based on NiO thin film on stainless steel, the MWCNT/NiO showed significant improvements because the vertically-aligned MWCNT arrays enabled easy ion and electron transport and acted as excellent base-structures that minimize pulverization of the active materials by absorbing the compressive and tensile stresses during charge and discharge processes. Electrochemical impedance spectroscopy of MWCNT/NiO showed low internal resistance and low charge-transfer resistance of the MWCNT/NiO that suggest superior ion and electron transport, respectively. This demonstrated that the vertically-aligned MWCNT array is a promising current collector for conversion-type active materials.

1. Introduction

Direct deposition/growth of active material on current collector is an interesting method to fabricate anode materials that undergo large volume changes during lithiation/delithiation. While this method does not use additional binder, it is able to minimize the pulverization of active material due to its unique structure [1-3]. In addition, it is in favor of easy electron transport and small lithium-ion diffusion distance. The current collector with a rough surface improves the anode performance due to the formation of sparse nanoparticles instead of smooth thin film of active material. Wang et al [1] showed that roughened nickel (Ni) foam substrate was a good current collector for a high rate capability. Fan et al [2] reported that Ni particle arrays were good current collectors with very good electrical contact properties. The vertically-aligned multiwall carbon nanotube (MWCNT) arrays with a relatively high aspect ratio and sparse spacing were found to be a promising current collector for lithium-ion battery electrode [3]. The high aspect ratio enabled the vertically-aligned MWCNT arrays to hold more active material than rough current collector, while the spacing between MWCNTs provided a room for expansion of the coated active material.

Nickel oxide (NiO) is a conversion-type anode material for lithium-ion batteries with a theoretical capacity of 718 mA h g^{-1}. It undergoes a conversion process where reduction/oxidation of NiO and formation/decomposition of lithium oxide (Li_2O) are reversible [4]. Some challenges of NiO anodes are : 1) pulverization due to the large volume change during lithiation/delithiation and 2) low electronic conductivity due to the semiconducting property of NiO with band gap of ~3.8 eV [5]. These challenging problems might be tackled by coating the NiO on vertically-aligned MWCNT arrays (MWCNT/NiO).

NiO can be fabricated by plasma-assisted oxidation [6], electrochemical deposition followed by oxidation [7], thermal evaporation followed by oxidation [8], pulsed laser deposition [9], reactive radio frequency sputtering [10], and thermal oxidation of Ni foam [11], etc. Chiu et al [10] deposited nanocrystalline NiO thin film using bias-sputter-deposition and achieved a specific

capacity of ~720 mA h g^{-1} up to 30 cycles. A discharge cut-off voltage of 0.5 V vs. Li/Li^+ was used to minimize pulverization. Xu et al [12] prepared NiO-MWCNT composites using direct thermal decomposition method. Their material showed a specific capacity of ~800 mA h g^{-1} after 50 discharge/charge cycles. To our knowledge, due to pulverization of the film during lithiation/delithiation, no report has ever presented a stable cycle performance of sputtered NiO in the potential window of 0.02 – 3 V vs. Li/Li^+. In addition, no one has demonstrated vertically-aligned MWCNTs as a key to minimize NiO pulverization. In this paper, we investigated the electrochemical properties of MWCNT/NiO samples where the NiO was deposited by direct current (DC) reactive sputtering method.

2. Experimental

2.1. Sample Preparation

The vertically-aligned MWCNT arrays were grown on 16.2 mm-diameter stainless steel (SS) disks purchased from Lee & Lim International. Initially SS disks were cleaned in an ultrasonic bath for 30 minutes in propan-2-ol and then dried inside vacuum oven at 80 °C for 4 hours. A thin titanium nitride (TiN) barrier layer was deposited using DC sputtering system of Elite Sputter. Then, 20 nm Ni film was deposited using electron-beam (E-beam) evaporation system of Edwards E-Beam Evaporation. After Ni deposition, the samples were placed inside a chamber of a plasma-enhanced chemical vapor deposition of Nanoinstruments Ltd system, with the base pressure of typically 3 Pa. The ammonia gas was flowed to maintain a pressure of 8.7×10^2 Pa. To dewet the Ni thin film into Ni nanoparticle arrays, the temperature was rapidly increased to 800 °C. Subsequently, to grow the vertically-aligned MWCNT arrays, 120 Watt plasma was switched on and the acetylene gas was flowed. The deposition time was 10 minutes.

To fabricate MWCNT/NiO, NiO was sputtered on vertically-aligned MWCNT arrays in a DC sputtering chamber of Elite Sputter. NiO was sputtered from a pure Ni target at 300 Watts. The argon and oxygen were flowed at 75 and 25 sccm, respectively. The base pressure and

deposition pressure were typically 4×10^{-4} and 1.2 Pa, respectively. The sputtering was carried out without substrate heating. For a comparison, NiO thin film on SS (SS/NiO) was also prepared under the same sputtering condition. The SS/NiO serves as a control sample. The NiO mass loading of both MWCNT/NiO and SS/NiO samples were 0.90 mg cm^{-2}, as measured by Mettler Toledo XP26 DeltaRange balance with readability of 0.002 mg.

2.2. Physical Characterization

The sputtered NiO was characterized using X-Ray Diffraction (XRD) of Siemens D5005 with Cu Kα of 0.1540 nm and θ of 3°. Raman Spectroscopy was performed using WITec with excitation wavelengths of 532 nm. The initial morphology of the samples was investigated using Scanning Electron Microscopy (SEM) of FEI Nova Nanolab DualBeam 600i with accelerating voltage of 5.00 kV. Using the same machine, the Focused Ion Beam (FIB) was used for the preparation of samples prior the cross-section SEM. Transmission Electron Microscopy (TEM) was performed using JEOL 2010 with accelerating voltage of 200 kV. The morphology of the samples after 50 cycles was characterized using LEO 1550 Gemini SEM with accelerating voltage of 5.00 kV.

2.3. Electrochemical Characterization

The samples, Celgard-2300 separators, liquid electrolytes and pure Li metals were assembled in 2032-type coin cells inside an argon glove box. The oxygen and moisture level inside the glove box were less than 5 ppm. The liquid electrolyte used was 1 M lithium hexafluorophosphate dissolved in 1:1 by volume of ethylene carbonate and diethyl carbonate. Battery cycle life testing and cyclic voltammetry were performed using Neware battery tester and Autolab machine, respectively.

Electrochemical impedance spectroscopy (EIS) was performed using Autolab machine at 0.01 V amplitude from 1×10^5 Hz to 0.22 Hz frequency. The discharge and charge referred to lithiation and delithiation, respectively. The 3rd cycle's discharge/charge at the rate of 0.05 C were

paused when EIS measurements were performed. The potentials were chosen at a regular interval for EIS measurements at 3, 2.7, 2.4, 2.1, 1.8, 1.5, 1.2, 0.9, 0.6, 0.3 and 0.02 V during discharge and 0.3, 0.6, 0.9, 1.2, 1.5, 1.8, 2.1, 2.4, 2.7 and 3 V during charge. All EIS data were verified using Kronig-Kramers algorithm.

3. Results and discussion

Successful coating of NiO was confirmed using XRD and Raman spectra. Fig. 1a shows the XRD pattern of MWCNT/NiO sample. There were noticeable shifts of the NiO peak to a lower value of 2θ. The NiO peaks at 37.0°, 43.0°, 62.3°, 62.5°, 75.1°, 78.6°, and 78.8° could be assigned to NiO (101), (012), (110), (104), (113), (202), and (006), respectively. The lattice spacing was slightly enlarged probably due to the formation of non-stoichiometric oxygen-rich NiO ($NiO_{y,\ where\ y>1}$) due to the creation of Ni vacancies or oxygen interstitial during sputtering [13-16]. The small shoulders could be attributed to the SS substrate with powder-diffraction-file number of 33-397. SS signals were detected because small area of the MWCNT/NiO sample was bare SS for easier handling during fabrication steps. Fig. 1b shows the Raman spectrum of MWCNT/NiO sample. The peak at about 515 cm^{-1} was caused by Ni-O stretching mode [17, 18]. The MWCNTs were not detected by XRD and Raman due the thick NiO coating. Fig. 1c shows the high resolution TEM image of NiO in the MWCNT/NiO sample. The fringe spacing of 0.242 nm was observed in Fig. 1c, corresponding to the (101) plane of NiO. The TiN and pure Ni signal were not detected by XRD analysis probably because they were 1) blocked by thick NiO and 2) very thin so that their signals were too weak to be detected. Although most MWCNTs were covered with thick NiO as shown in Fig. 1d, we managed to observe the Ni catalyst using TEM as shown in Fig. 1e.

The SEM images of SS substrate, MWCNT array, SS/NiO sample and MWCNT/NiO sample are displayed in Fig. 2. The SS had a relatively smooth microstructure as shown in Fig. 2a and 2b. After growing the vertically-aligned MWCNT arrays, the microstructure became relatively rough as seen in Fig. 2c and 2d. The MWCNT arrays were seen protruding out with an angle normal to the surface in Fig. 2d. The rough microstructure of the substrate is a desirable

feature to minimize pulverization of NiO during lithiation/delithiation [2]. A significant difference of the morphologies of SS/NiO and MWCNT/NiO samples can be seen in Fig. 2e to 2h. Fig. 2e and 2f show the deposited NiO film on the SS/NiO sample had a relatively smooth film. In contrast, Fig. 2g and 2h show the deposited NiO film on MWCNT/NiO sample had a relatively disperse NiO particles with spacing between them. Using FIB machine, a protective layer was deposited locally prior to FIB milling. The purpose of introducing the protective layer was to prevent the damage on the area-of-interest during FIB milling. The FIB milling operation was performed adjacent to the area-of-interest to reveal the cross-section of the structure. The NiO particles were attached to the vertically-aligned MWCNT arrays on the SS current collector as shown from the cross-section SEM image of Fig. 2i and 2j. The average height of the vertically-aligned MWCNT arrays with NiO coating of the MWCNT/NiO sample was 5.97 μm. Although we did not perform the cleaning after FIB process, the redeposition of the milled material was negligible since the depth and the width of the hole were comparable. Most of the milled material was sucked by the vacuum system.

Battery testing performance of MWCNT/NiO sample, SS/NiO sample, and MWCNT substrate at the rate of 143.6 mA g^{-1} is shown in Fig. 3a. All capacities were normalized with NiO mass. For the MWCNT/NiO sample, the first cycle's specific discharge capacity, specific charge capacity and Coulombic efficiency were 1146.3 mA h g^{-1}, 863.2 mA h g^{-1} and 75.3%, respectively. The corresponding values for the second cycle were 865.4 mA h g^{-1}, 841.9 mA h g^{-1} and 97.3%. The specific discharge capacity was stable from the 2^{nd} to 50^{th} cycle at about 864.8 mA h g^{-1}. In contrast, the SS/NiO sample showed apparent degradation with a specific discharge capacity of 285.9 mA h g^{-1} at the 50th cycle. The specific capacity contributed from the vertically-aligned MWCNTs was only 21.1 mA h g^{-1}. It was negligible to the overall specific capacity of MWCNT/NiO sample.

The experimental specific discharge capacity of MWCNT/NiO of 864.8 mA h g^{-1} was higher than the NiO theoretical specific capacity of 718 mA h g^{-1}. This could be tentatively

attributed to 1) the contribution from polymeric gel-like film resulting from kinetically activated electrolyte degradation [19-21] and 2) the $NiO_{y,\ where\ y>1}$ has a higher theoretical specific capacity than NiO. The electrochemical reaction for $NiO_{y,\ where\ y>1}$ was modified from stoichiometric NiO [22]:

$$NiO_{y,\,where\,y>1} + 2y\,Li^{+} + 2y\,e^{-} \underset{charge}{\overset{discharge}{\rightleftharpoons}} Ni + y\,Li_2O \qquad \text{Equation (1)}$$

$$\text{The theoretical specific capacity of } NiO_{y,where\,y>1}$$

$$= \frac{\text{no. of electron transfer} \times \text{Faraday constant}\left(\text{A}.\frac{\text{s}}{\text{mol}}\right)\times 1000\left(\frac{\text{mA}}{\text{A}}\right)}{NiO_{y,\,where\,y>1}\ \text{mass}\left(\frac{\text{g}}{\text{mol}}\right)\times 3600\left(\frac{\text{s}}{\text{h}}\right)}$$

$$= \frac{2y \times 96485.3365 \times 1000}{(58.693 + 15.999y)\times 3600} \qquad \text{Equation (2)}$$

$$\text{The theoretical specific capacity of NiO} = \frac{2 \times 96485.3365 \times 1000}{(58.693 + 15.999)\times 3600} \qquad \text{Equation (3)}$$

$$\frac{\text{The theoretical specific capacity of } NiO_{y,where\,y>1}}{\text{The theoretical specific capacity of NiO}} = \frac{74.692y}{(58.693 + 15.999y)} > 1 \qquad \text{Equation (4)}$$

The theoretical specific capacity of $NiO_{y,\ where\ y>1}$ is always higher than that of NiO as shown in equation 4. In this study, the mass measurement error was negligible, considering the high resolution of the mass balance and no significant side reaction during sputter deposition of NiO at room temperature.

Fig. 3b shows the specific capacities of the MWCNT/NiO sample, SS/NiO sample, and MWCNT substrate. Different charge and discharge rates were programmed each for 10 cycles at the rate of 0.1, 0.2, 0.5, and 1 C (1 C = 718 mA g^{-1}). The MWCNT/NiO sample showed a relatively stable specific capacity of 958.2, 936.6, 889.7, and 820.1 mA h g^{-1} at the rate of 0.1, 0.2, 0.5, and 1 C, respectively. In contrary, the SS/NiO sample showed a degraded specific capacity of 398.6, 293.7, 215.1 and 159.2 mA h g^{-1} at the rate of 0.1, 0.2, 0.5, and 1 C, respectively. The MWCNT specific capacity was only 22.5, 19.8, 16.1 and 13.4 mA h g^{-1} at 0.1, 0.2, 0.5, and 1 C rate, respectively. After the rate was returned back to 0.1 C, the MWCNT/NiO sample showed a

significant recovery compared with the SS/NiO sample. These results indicate that the MWCNT/NiO sample did have much better performance than the SS/NiO sample. The vertically-aligned MWCNT arrays must play important roles in enhancing the electronic paths, absorbing the compressive and tensile stresses, and minimizing NiO pulverization during lithiation/delithiation.

The first cycle's discharge voltage profile of the MWCNT/NiO sample shown in Fig. 3c was different from the subsequent discharge voltage profile probably due to the drastic lithium driven, structural or textural modifications [23, 24]. Fig. 3d shows the cyclic voltammetry of MWCNT/NiO sample at a scan rate of 0.1 mV s^{-1} and a potential window of 0.02 – 3.0 V. In the first cycle, a peak at around 0.45 V and a shoulder at around 0.5 V could result from initial reduction of NiO to Ni nanoparticles and a formation of amorphous Li_2O and solid electrolyte interface (SEI) [7, 25, 26]. During the first anodic scan, the peaks at around 1.50 and 2.25 V could be attributed to SEI decomposition, NiO formation and Li_2O decomposition [26, 27]. On the subsequent cycles, the cathodic scan peak stabilized at around 0.96 V with a shoulder at around 1.1 V and the anodic scan peak stabilized at 2.25 V with a weak peak at 1.50 V.

Compared to NiO-MWCNT composites using direct thermal decomposition method [12], our structure has two advantages: 1) Our MWCNT/NiO sample contained vertically-aligned MWCNT arrays which directly grown on the current collector. The direct connection offered an advantage of easy electron transport from NiO to the current collector. 2) Our MWCNT/NiO sample featured a relatively regular spacing between vertically-aligned MWCNTs. It enabled easy ion transport due to easy access of electrolyte to the active material. The spacing also acted as a room to accommodate the expansion/contraction of NiO during lithiation/delithiation. These advantages enabled our structure to have a stable cycle performance at the rate of 143.6 mA g^{-1} for 50 cycles and an ability to be discharged/charged at higher rates up to 718 mA g^{-1} as shown in Fig. 3a and 3b, respectively. In contrast, reference [12] showed the battery characterization at a small rate of 50 mA g^{-1}.

The superior electron and ion transport of MWCNT/NiO were studied using EIS. Fig. 4a and 4b represent the typical Nyquist plot generated from EIS measurements. Each point in the Nyquist plot corresponds to EIS measurement at a specific frequency where high to low frequencies were presented from left to right. The x and y axis correspond to the real and imaginary value of the impedance, respectively. The small semicircle at higher frequencies is related to the formation of SEI film, while the semicircle at medium frequency is related to the charge-transfer resistance on electrode/electrolyte interface [28, 29]. The inclined line at the lower frequencies is related to the diffusion of lithium ions [29]. Internal resistance and charge-transfer resistance could be extracted from the Nyquist plots. Fig. 4c and 4d summarized the internal resistance and charge-transfer resistance of SS/NiO and MWCNT/NiO, respectively.

Barsukov and Qian [30] suggested that low frequency impedance measurement could determine the internal resistance more accurately than 1 kHz high frequency impedance measurement. In our set-up, the lowest frequency we achieved for valid EIS data was 0.22 Hz, which corresponds to the relaxation time of 4.55 s. Fig. 4c shows the resistance at 0.22 Hz was a function of the potential during discharge and charge process. This was comparable to the variation of resistance with the state-of-charge in reference [30]. The resistances of the MWCNT/NiO sample varied in the range of 62.2 Ω (at 0.6 V discharge) to 228 Ω (at 2.1 V discharge). In contrast, the resistances of SS/NiO samples varied greatly from 130.8 Ω (at 0.3 V discharge) to 1653.8 Ω (at 3 V charge). The resistances of MWCNT/NiO were smaller than the resistances of SS/NiO in all potentials. The difference of the resistances was the highest of 1517.3 Ω (at 3 V charge) and the lowest of 30.3 Ω (at 0.3 V charge). The difference was less significant at lower potentials probably due to domination of charge-transfer resistance at lower potentials. Since the resistance at low frequencies is related to the diffusion component of the Li-ion, this shows that the MWCNT/NiO has better ion transport than SS/NiO in all potential. Fig. 4d shows the charge-transfer resistance of SS/NiO and MWCNT/NiO samples. The MWCNT/NiO sample had lower charge-transfer resistances than SS/NiO sample in all potentials. The charge-transfer

resistance was dominated at lowest potential of 0.02 V. Since the charge-transfer resistance is related with the electron transport, this shows that the MWCNT/NiO has better electron transport than SS/NiO. The superior rate capability of MWCNT/NiO is probably caused by better ion and electron transport as indicated by low internal resistance and low charge-transfer resistance, respectively.

The structure of the MWCNT/NiO and SS/NiO after 50 cycles was investigated using SEM. Fig 5a shows the morphology of MWCNT/NiO before and after 50 cycles. After being cycled, the MWCNT/NiO surface showed different morphology: from disperse NiO particles to relatively smooth surface. This could be explained by the structural change during the first lithiation when NiO structure was converted to Ni nanoparticles-inside-Li_2O and gel-like matrixes [23, 24]. Unlike alloying-type materials that simply expand during lithiation [3], the conversion-type material involves reduction of the metal oxides to metal nanoparticles and formation of Li_2O and SEI matrixes during lithiation [7, 25, 26]. After 50 cycles, MWCNT/NiO also showed relatively uniform inter-cracks between the active materials but still remained stable structures across a large area, as shown in Fig. 5b and 5c, which is similar with the finding in reference [3]. In contrast, the SS/NiO showed large irregular cracks as shown in Fig 5d and 5e. The optical photograph of MWCNT/NiO and SS/NiO after 50 cycles evidenced that the active material film of SS/NiO sample was easily peeled-off due to pulverization of the active material and weak adhesion of the active material to SS. In contrary, these problems did not occur in the MWCNT/NiO samples. The MWCNT/NiO structure remained stable mainly due to 1) the vertically-aligned MWCNT arrays acted as buffers that provided strain relaxation and volume change accommodation and 2) the strong adhesion of the active materials to vertically-aligned MWCNT arrays.

4. Conclusion

We have successfully fabricated high performance MWCNT/NiO anode for lithium-ion batteries. The MWCNT/NiO structure was prepared by sputtering Ni target in argon and oxygen

ambient onto vertically-aligned MWCNT arrays on SS. A specific capacity of 864.8 mA h g^{-1} was achieved after 50 cycles at a rate of 143.6 mA g^{-1}. The high performance can be attributed to the unique MWCNT/NiO structure in which vertically-aligned MWCNTs enhance the ion and electron transport, absorb both the compressive and tensile stresses and minimize NiO pulverization during lithiation/delithiation. EIS study of MWCNT/NiO showed low internal and charge-transfer resistance that suggest superior ion and electron transport, respectively. SEM of MWCNT/NiO after 50 cycles evidenced stable structures across a large area. The combination of vertically-aligned MWCNT arrays with conversion-type anode active material is a promising anode material for Li-ion batteries.

Acknowledgements

The first author acknowledged the financial support by the Singapore-MIT Alliance (SMA) under the Flagship Research Program (FRP). We acknowledged Lu Congxiang and Wahyuaji Narottama Putra for help in MWCNT fabrication and SEM/FIB characterization, respectively. This work is also partially supported by MOE AcRF Tier2 Funding, Singapore. (MOE2011-T2-1-137)

References

[1] Wang X, Yang Z, Sun X, Li X, Wang D, Wang P, et al. NiO nanocone array electrode with high capacity and rate capability for Li-ion batteries. Journal of Materials Chemistry. 2011;21(27):9988-90.

[2] Fan Y, Huang K, Zhang Q, Xiao Q, Wang X, Chen X. Novel silicon-nickel cone arrays for high performance LIB anodes. Journal of Materials Chemistry. 2012;22(39):20870-3.

[3] Fan Y, Zhang Q, Xiao Q, Wang X, Huang K. High performance lithium ion battery anodes based on carbon nanotube-silicon core-shell nanowires with controlled morphology. Carbon. 2013;59:264-9.

[4] Poizot P, Laruelle S, Grugeon S, Dupont L, Tarascon JM. Searching for new anode materials for the Li-ion technology: Time to deviate from the usual path. Journal of Power Sources. 2001;97-98:235-9.

[5] Adler D, Feinleib J. Electrical and optical properties of narrow-band materials. Physical Review B. 1970;2(8):3112-34.

[6] Varghese B, Reddy MV, Yanwu Z, Lit CS, Hoong TC, Rao GVS, et al. Fabrication of NiO nanowall electrodes for high performance lithium ion battery. Chemistry of Materials. 2008;20(10):3360-7.

[7] Wang H, Pan Q, Wang X, Yin G, Zhao J. Improving electrochemical performance of NiO films by electrodeposition on foam nickel substrates. Journal of Applied Electrochemistry. 2009;39(9):1597-602.

[8] Nuli YN, Zhao SL, Qin QZ. Nanocrystalline tin oxides and nickel oxide film anodes for Li-ion batteries. Journal of Power Sources. 2003;114(1):113-20.

[9] Wang Y, Qin QZ. A nanocrystalline NiO thin-film electrode prepared by pulsed laser ablation for Li-ion batteries. Journal of the Electrochemical Society. 2002;149(7):A873-A8.

[10] Chiu KF, Chang CY, Lin CM. The electrochemical performance of bias-sputter-deposited nanocrystalline nickel oxide thin films toward lithium. Journal of the Electrochemical Society. 2005;152(6):A1188-A92.

[11] Wang X, Li X, Sun X, Li F, Liu Q, Wang Q, et al. Nanostructured NiO electrode for high rate Li-ion batteries. Journal of Materials Chemistry. 2011;21(11):3571-3.

[12] Xu C, Sun J, Gao L. Large scale synthesis of nickel oxide/multiwalled carbon nanotube composites by direct thermal decomposition and their lithium storage properties. Journal of Power Sources. 2011;196(11):5138-42.

[13] Yoshimura K, Miki T, Tanemura S. Nickel oxide electrochromic thin films prepared by reactive DC magnetron sputtering. Japanese Journal of Applied Physics, Part 1: Regular Papers & Short Notes & Review Papers. 1995;34(5 A):2440-6.

[14] Andersson AM, Estrada W, Granqvist CG, Gorenstein A, Decker F. Characterization of electrochromic dc-sputtered nickel-oxide-based films. p. 96-110.

[15] Jang WL, Lu YM, Hwang WS, Chen WC. Electrical properties of Li-doped NiO films. Journal of the European Ceramic Society. 2010;30(2):503-8.

[16] Yang JL, Lai YS, Chen JS. Effect of heat treatment on the properties of non-stoichiometric p-type nickel oxide films deposited by reactive sputtering. Thin Solid Films. 2005;488(1-2):242-6.

[17] Li X, Dhanabalan A, Bechtold K, Wang C. Binder-free porous core-shell structured Ni/NiO configuration for application of high performance lithium ion batteries. Electrochemistry Communications. 2010;12(9):1222-5.

[18] Cordoba-Torresi SI, Hugot-Le Goff A, Joiret S. Electrochromic behavior of nickel oxide electrodes. II. Identification of the bleached state by Raman spectroscopy and nuclear reactions. Journal of the Electrochemical Society. 1991;138(6):1554-9.

[19] Grugeon S, Laruelle S, Dupont L, Tarascon JM. An update on the reactivity of nanoparticles co-based compounds towards Li. Solid State Sciences. 2003;5(6):895-904.

[20] Do JS, Weng CH. Preparation and characterization of CoO used as anodic material of lithium battery. Journal of Power Sources. 2005;146(1-2):482-6.

[21] Zhou G, Wang DW, Li F, Zhang L, Li N, Wu ZS, et al. Graphene-wrapped Fe3O4 anode material with improved reversible capacity and cyclic stability for lithium ion batteries. Chemistry of Materials. 2010;22(18):5306-13.

[22] Wang X, Song J, Gao L, Jin J, Zheng H, Zhang Z. Optical and electrochemical properties of nanosized NiO via thermal decomposition of nickel oxalate nanofibres. Nanotechnology. 2005;16(1):37-9.

[23] Wang C, Wang D, Wang Q, Chen H. Fabrication and lithium storage performance of three-dimensional porous NiO as anode for lithium-ion battery. Journal of Power Sources. 2010;195(21):7432-7.

[24] Poizot P, Laruelle S, Grugeon S, Dupont L, Tarascon JM. Nano-sized transition-metal oxides as negative-electrode materials for lithium-ion batteries. Nature. 2000;407(6803):496-9.

[25] Pan Q, Liu J. Facile fabrication of porous NiO films for lithium-ion batteries with high reversibility and rate capability. Journal of Solid State Electrochemistry. 2009;13(10):1591-7.

[26] Grugeon S, Laruelle S, Herrera-Urbina R, Dupont L, Poizot P, Tarascon JM. Particle Size Effects on the Electrochemical Performance of Copper Oxides toward Lithium. Journal of the Electrochemical Society. 2001;148(4):A285-A92.

[27] Débart A, Dupont L, Poizot P, Leriche JB, Tarascon JM. A Transmission Electron Microscopy Study of the Reactivity Mechanism of Tailor-Made CuO Particles toward Lithium. Journal of the Electrochemical Society. 2001;148(11):A1266-A74.

[28] Kang Y-M, Song M-S, Kim J-H, Kim H-S, Park M-S, Lee J-Y, et al. A study on the charge–discharge mechanism of Co3O4 as an anode for the Li ion secondary battery. Electrochimica Acta. 2005;50(18):3667-73.

[29] Yang S, Song H, Chen X. Electrochemical performance of expanded mesocarbon microbeads as anode material for lithium-ion batteries. Electrochemistry Communications. 2006;8(1):137-42.

[30] Barsukov Y, Qian J. Battery power management for portable devices. Boston: Artech House; 2013.

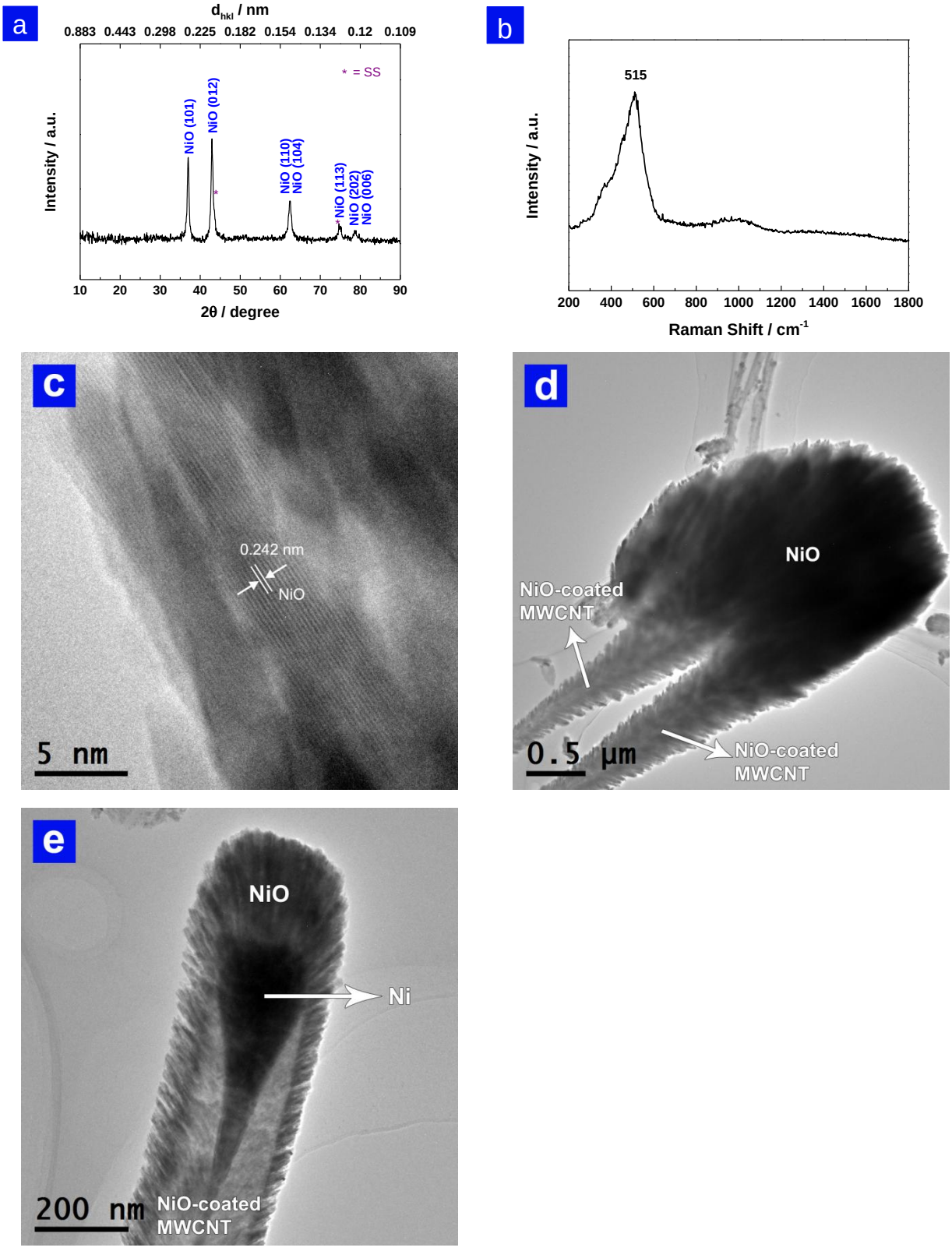

Fig. 1 – (a) The XRD spectrum and (b) The Raman spectrum of MWCNT/NiO sample. (c) The High Resolution TEM image of NiO in the MWCNT/NiO sample. The TEM images of MWCNT/NiO sample showing (d) thick-NiO-coated MWCNT and (e) thin-NiO-coated MWCNT.

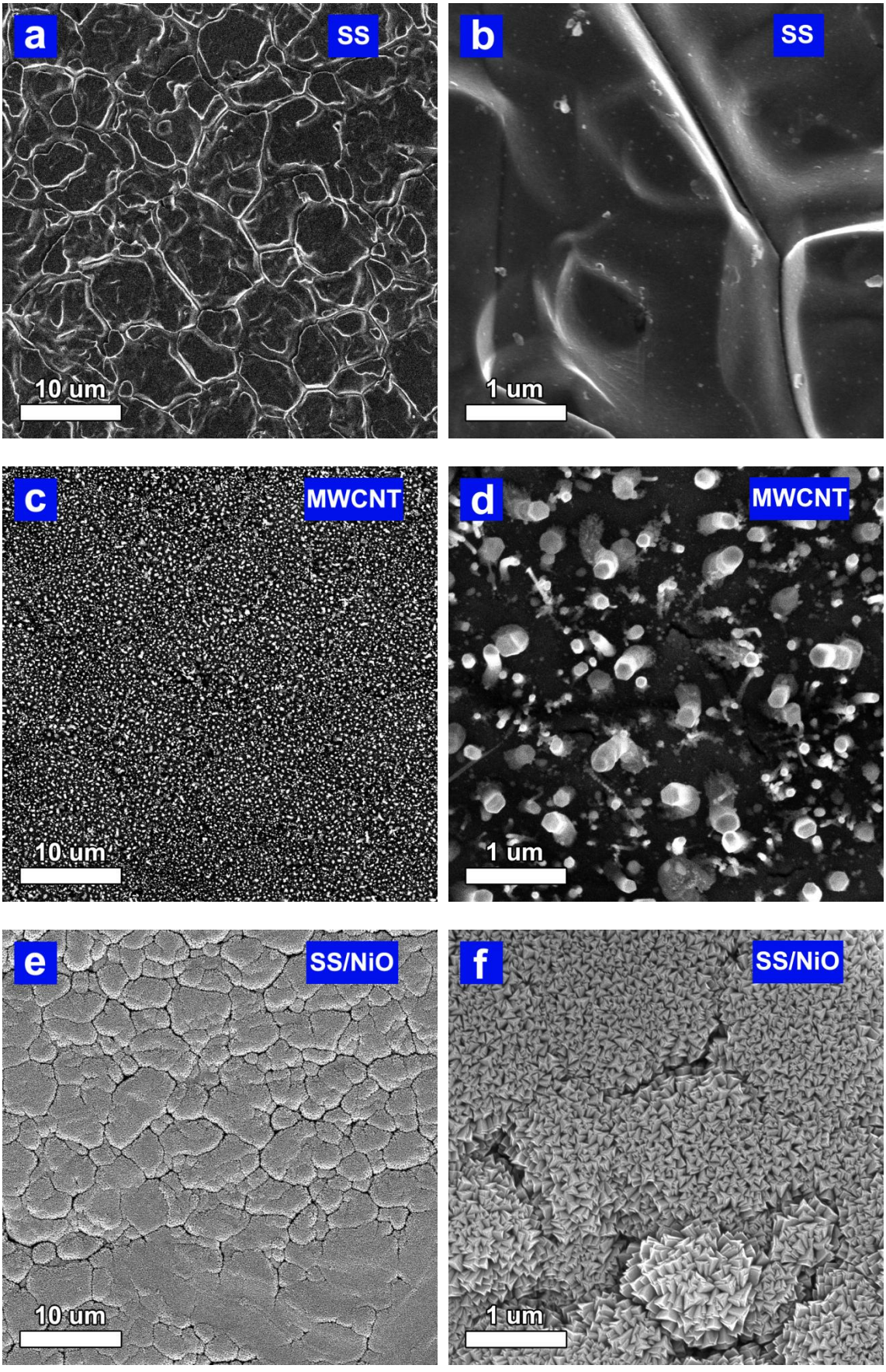
a
SS
10 um
b
SS
1 um
c
MWCNT
10 um
d
MWCNT
1 um
e
SS/NiO
10 um
f
SS/NiO
1 um

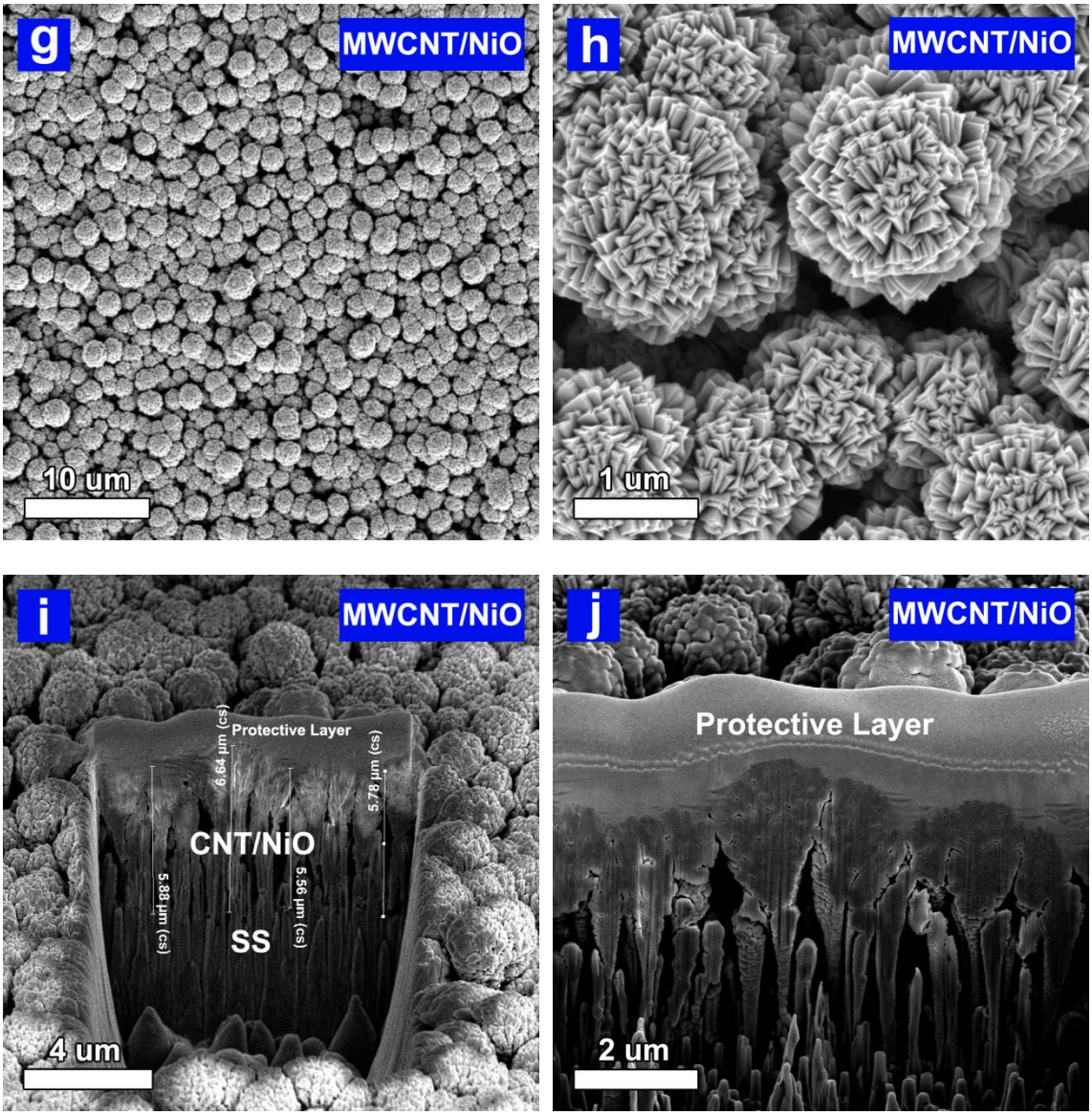

Fig. 2 – The SEM images of (a, b) SS substrate; (c, d) vertically-aligned MWCNT array; (e, f) SS/NiO sample; (g, h) MWCNT/NiO sample and (i, j) cross-section of MWCNT/NiO sample.

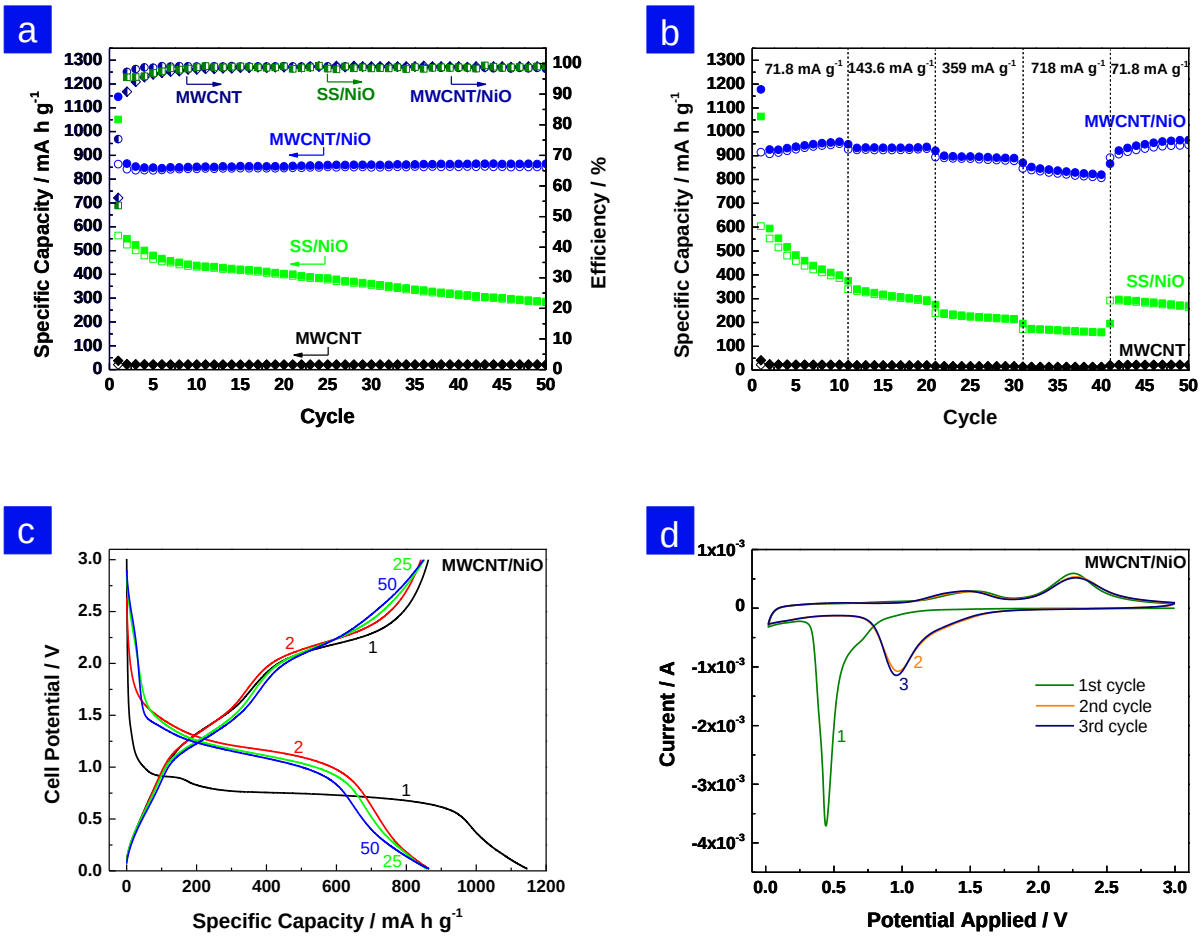

Fig. 3 – (a) The specific capacity vs. cycle number and (b) the rate capabilities of the MWCNT/NiO, SS/NiO and MWCNT samples. (c) The cell potential vs. specific capacity of the MWCNT/NiO sample at 1st, 2nd, 25th and 50th cycle. (d) The Cyclic voltammetry of the MWCNT/NiO sample at 1st, 2nd, and 3rd cycle.

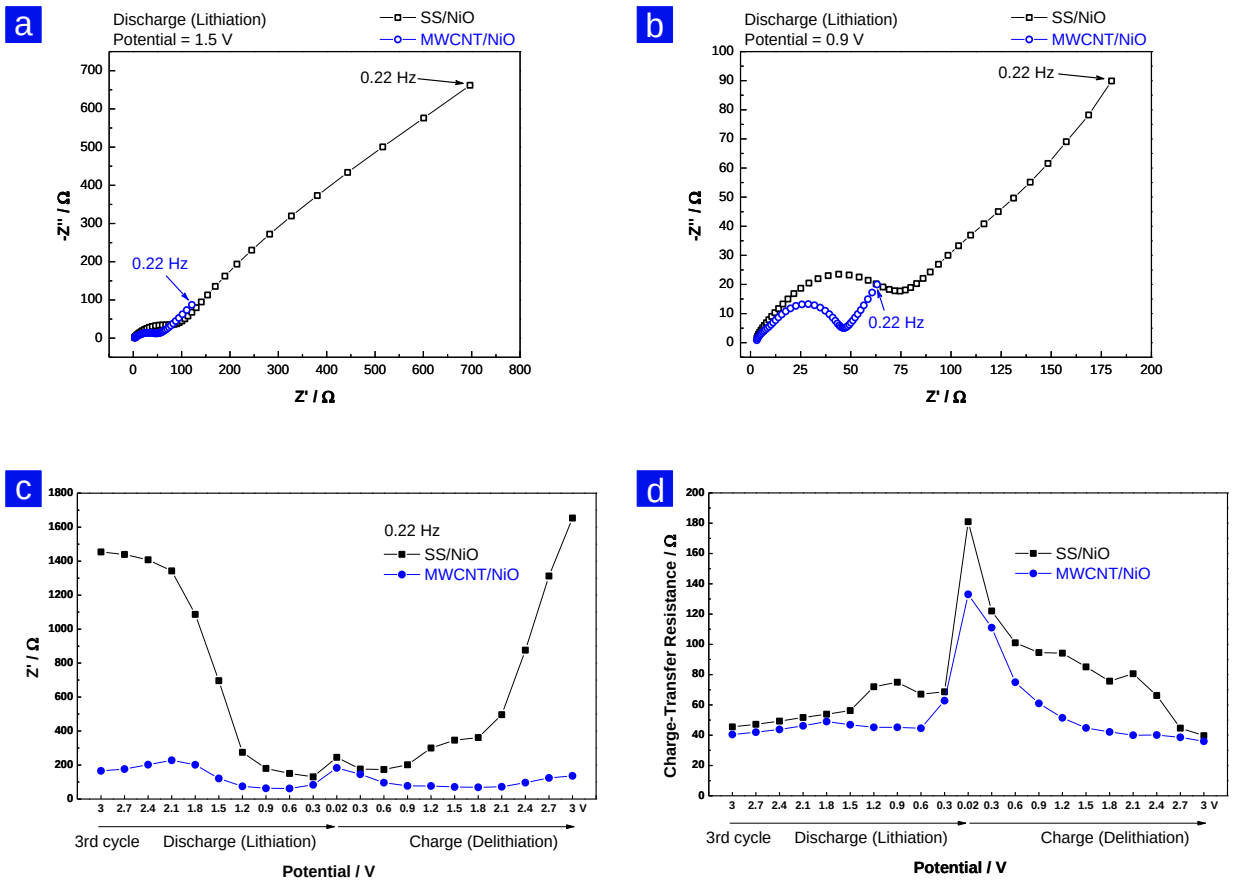

Fig. 4 – The Nyquist plot of SS/NiO and MWCNT/NiO samples during 3rd cycle's discharge at (a) 1.5 V and (b) 0.9 V. (c) The resistance at 0.22 Hz and (d) the charge-transfer resistance during 3rd cycle's discharge and charge of SS/NiO and MWCNT/NiO samples.

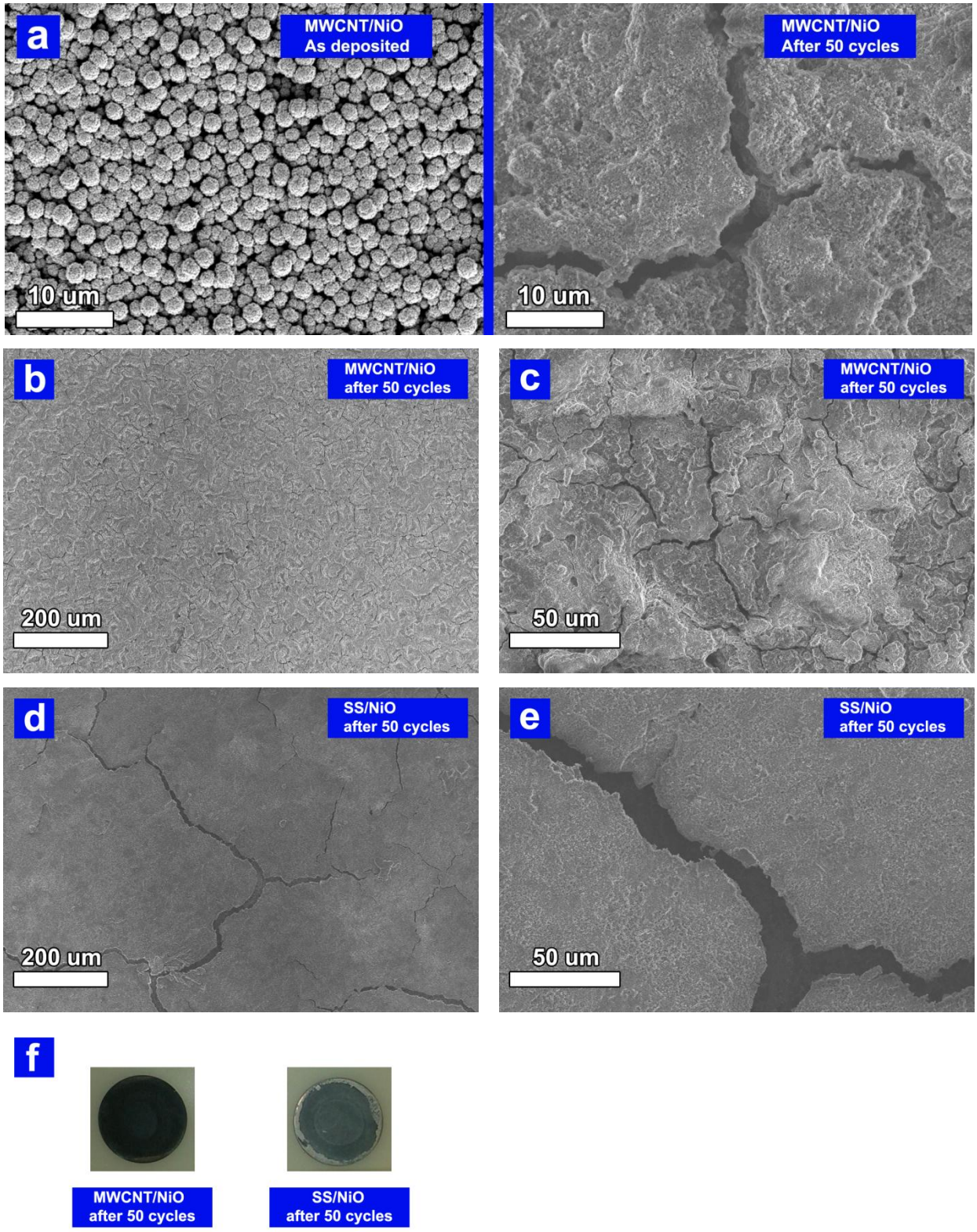

Fig. 5 – (a) The SEM images of MWCNT/NiO before cycling and after 50 cycles. The SEM images of (b, c) MWCNT/NiO and (d, e) SS/NiO after 50 cycles at different magnification. (f) The pictures of MWCNT/NiO and SS/NiO after 50 cycles.